The Finite-Element Method Contrast Source Inversion Algorithm for 2D Transverse Electric Vectorial Problems

Amer Zakaria, *Member, IEEE*, and Joe LoVetri, *Senior Member, IEEE*

***Abstract*—The contrast source inversion algorithm is formulated using the finite-element method for two-dimensional transverse electric microwave imaging problems. Edge-based triangular elements with vector basis functions are utilized to solve the TE electromagnetic problem. A single finite-element method (FEM) mesh is used to model both the electric field as well as the contrast-source and contrast variables used in the inverse problem. The electromagnetic field is modeled by taking the unknown values to be the tangential components of the transverse electric field along the edges of each triangular element. The unknown contrast-source and contrast variables are located at the centroids of every triangular element of the same FEM mesh, but only inside the imaging domain. The adaptation of the FEM-contrast source inversion (FEM-CSI) algorithm to 2D-TE problems on such an arbitrary mesh requires the implementation of special transformation operators which are presented herein. The algorithm's capabilities are demonstrated by inverting the Fresnel experimental TE datasets as well as synthetically generated data.**

***Index Terms*—Contrast source inversion (CSI), finite-element method (FEM), microwave imaging, transverse-electric.**

I. INTRODUCTION

MICROWAVE imaging (MWI) is a modality where one is interested in determining some unknown attributes of an object-of-interest (OI) by utilizing electromagnetic fields measured outside the OI. These attributes are the location, shape, and electrical properties (i.e., permittivity and/or conductivity) of the OI. The object is located inside an imaging domain with known "background" electrical properties and is interrogated by sources of electromagnetic radiation emitting from a multitude of locations. For each source the presence of the object, having different electrical properties than the background, results in a scattered field that is measured at various locations surrounding the object. These measurements, once calibrated, constitute the data that is inverted by the imaging algorithm to reconstruct an image of the electrical properties. Tomographic imaging algorithms, which image 2D cross-sections of the OI, have proven their usefulness in several microwave imaging configurations where 3D systems can be well approximated as a 2D electromagnetic inverse problem [1]–[3].

Part of the design of an MWI system, which allows the imaging process to be successfully approximated as a 2D inverse problem, is deciding which polarization of electromagnetic radiation will be predominantly maintained. For biomedical imaging purposes, MWI has mostly been implemented using the transverse magnetic (TM) polarization [1], [4]–[6]. Based on a numerical investigation, it has been shown that using the transverse electric (TE) polarization in the near-field can result in more accurate reconstructions than interrogating the OI with the TM polarization [7]. Although 2D-TE imaging algorithms exist [7], [8], the new multiplicative regularized contrast source inversion (MR-CSI) algorithm presented herein, which is formulated using the finite element method (FEM), has all of the novel features presented in the MR-FEM-CSI algorithm which was recently presented for the TM case [9], [10]. The extension to the TE case is non-trivial because the problem changes from a scalar electromagnetic field problem to a vector field problem.

Of course, scalar as well as full-vectorial 3D imaging algorithms have been available for some time (see, e.g., [11]), and there are groups working to build such systems [12], [13], but, to the best of our knowledge, there are currently no 2D-TE biomedical imaging systems. The imaging lab at the University of Manitoba is currently working on such a 2D-TE system prior to embarking on a 3D full-vectorial system. The algorithm presented herein can be easily extended to the 3D full-vectorial case. The main differences between a 2D TE and a 3D full-vectorial inversion algorithm are minimal from a formulation point of view, but, of course, the latter will require a substantially greater amount of computing resources [14].

The inverse scattering problem associated with MWI can be cast as an optimization problem over variables representing the unknown properties which are to be reconstructed. The nonlinearity and ill-posedness of this type of optimization problem have been successfully treated using various optimization and regularization techniques which together constitute the inversion algorithm [1], [7], [11], [15]–[21]. Examples of MWI inversion algorithms are the distorted Born iterative method [15], the Gauss-Newton inversion (GNI) [22], and the conjugate gradient technique applied to an FEM discretization of the problem [23]. In the so-called modified-gradient method (MGM) [24] one minimizes a cost functional in terms of both the scattered fields outside the OI, which are compared to the

---

Manuscript received June 23, 2011; revised January 20, 2012; accepted May 11, 2012. Date of publication July 10, 2012; date of current version October 02, 2012. This work was supported by Natural Sciences and Engineering Research Council of Canada, the University of Manitoba Graduate Fellowship, the Government of Manitoba Graduate Scholarship, and the Edward R. Toporeck Graduate Fellowship.

The authors are with the Department of Electrical and Computer Engineering, University of Manitoba, Winnipeg, MB R3T 5V6 Canada (e-mail: Joe_LoVetri@umanitoba.ca).

Color versions of one or more of the figures in this paper are available online at http://ieeexplore.ieee.org.

Digital Object Identifier 10.1109/TAP.2012.2207324

measured values, and the total field inside the imaging domain, which is expected to be consistent with the estimated dielectric properties. An interesting aspect of the MGM is that no forward solver is called during the iterations; the functional is formulated solely in terms of matrix-vector products. In addition to these local optimization techniques global techniques have also been used [19].

A state-of-the-art modified-gradient type technique that has had much success in solving inverse scattering problems is the MR-CSI method. The matrix operators utilized in the CSI methods that have been presented have been formulated in various ways. The originally published algorithm makes use of an integral-equation formulation of the electromagnetic field operators based on infinite domain homogeneous medium Green's function integrals [25], [26]. Although initially having been formulated only for two-dimensional (2D) transverse magnetic (TM) problems, which result in the use of a scalar Green's function, these have been extended to 2D transverse electric (TE) [8], [27] and full 3D vectorial problems via the use of Dyadic Green's functions [28]. In addition to these, techniques based on finite-difference discretizations of the Helmholtz operator [29], and even eigenfunction representations of the field operators [30] have been used. An important advantage of working with discretizations of partial differential equation (PDE) formulations of the associated field problem is that an inhomogeneous background can be used for the inverse problem, and arbitrarily-shaped conductive boundaries of the MWI chamber can be modeled, without requiring one to first obtain the Green's function for such a background and associated boundary conditions (which may not be possible in closed-form).

The advantages of using PDE formulations in CSI have been highlighted recently by formulating CSI and MR-CSI using the finite-element method (FEM) for 2D-TM problems [9], [10]. The FEM formulation of the inverse problem allows one to distribute the unknown electrical properties along an unstructured triangular mesh, and allows one to easily handle problems with arbitrary boundary types and shapes. The extension of this work to 2D TE problems, including multiplicative regularization of the inverse problem, is the subject of this paper. There are two standard approaches to formulate the electromagnetic problem for this extension. The first is to formulate the TE problem as a scalar problem using a single magnetic field component. As concluded in [14], such a formulation results in a less stable algorithm with degraded performance as compared to the second approach which formulates the problem in terms of the two electric field components in the transverse plane. Further, as discussed in [31], the numerical modeling of dielectric discontinuities is more difficult for TE problems formulated in terms of the longitudinal magnetic field component due to the difficulty of modeling polarization charges. Thus, the second standard approach which uses the vector electric field in the transverse plane has been chosen and is described herein.

For solving vectorial problems using FEM, the use of nodal-based elements exhibits shortcomings that can be overcome with the use of edge-based elements [32]–[34]. Edge-based elements were first introduced by Whitney [35], and later discussed by Nédélec for their use in applications that solve Maxwell's equations [36]. Edge-based elements (associated with vector basis functions) eliminate spurious modes that can introduce errors in field calculations for near-field problems; these erroneous modes were observed by Csendes and Silvester when a vectorial problem was solved using nodal-basis functions [37]. In addition, with edge-based elements the tangential field continuity along the element boundaries is guaranteed which is important at the interface between dielectric discontinuities. Edge-based elements are thus standardly used for 2D, as well as for 3D, vectorial problems.

In this paper, the CSI algorithm is formulated using edge-based elements in FEM for the 2D TE inverse problem. This formulation retains all of the advantages of its 2D TM counterpart, nevertheless there are several important differences which make the implementation not straight forward. The electric field values are calculated along the edges of each element in the triangular mesh with vector edge basis functions used to expand the field; this is different from the 2D TM case where the discretized field variables are located at the mesh nodes with the field being expanded using scalar nodal basis functions. The methods also differ on the way the unknown reconstruction variables used in CSI are represented. The contrast is related to the electrical properties of the OI, while the contrast source is the product of the contrast and the total electric field. Thus, for the 2D TE case, the contrast source variable is a spatial vector with two components in the transverse plane, whereas the contrast variable remains a scalar quantity. For the 2D TE case presented herein the unknown contrast and contrast-source variables are located at the centroids of the triangular elements while for the 2D TM case these variables are located at the nodes.

Thus, the FEM-CSI algorithm for 2D TE configurations requires the implementation of several specialized operators. For example, one operator takes the contrast-source at the centroids of elements inside the imaging domain to the scattered electric field along the edges of mesh elements. A second operator is implemented which calculates the scattered field vector anywhere inside the imaging domain, or on the measurement surface, from the scattered field values along element edges. The CSI algorithm, which updates the contrast and contrast-source variables, can be more simply implemented and described in terms of these operators.

The paper is arranged as follows. The mathematical problem and its discretization using edge-based FEM are outlined in Sections II and III. The description of the inversion algorithm is given in Section IV. The inversion results using experimental and synthetic datasets are shown and discussed in Section V. Finally, the paper is closed with a brief conclusion in Section VI.

II. PROBLEM STATEMENT

In the 2D TE configuration considered here we assume the electric field is polarized in the transverse x-y plane of the problem with no longitudinal component. All fields are considered time-harmonic with an $\exp(j\omega\tau)$ time-dependency, where ω is the radial frequency, τ is the time variable and $j^2 = -1$. The OI is located within an imaging domain, $\mathcal{D}$, with a background permittivity ϵ_b. The imaging domain is located within the problem domain, Ω, that is confined by a bounding surface Γ. The surface Γ can be either a radiating surface or a conducting enclosure; in the later case, the boundary can take any shape. The OI has a complex relative permittivity $\epsilon_r(\boldsymbol{r})$ where $\boldsymbol{r} = (x, y)$ is the 2D position vector. The electrical contrast of the OI is defined as $\chi(\boldsymbol{r}) = (\epsilon_r(\boldsymbol{r}) - \epsilon_b(\boldsymbol{r}))/\epsilon_b(\boldsymbol{r})$; outside $\mathcal{D}$, $\chi(\boldsymbol{r}) = 0$.

The imaging domain is illuminated by one of a total of T transmitters, producing a TE incident field $\vec{E}_t^{\text{inc}} = E_{t,x}^{\text{inc}}\hat{x} + E_{t,y}^{\text{inc}}\hat{y}$, defined as the field when there is no OI in $\mathcal{D}$. In the presence of the OI, the total field vector $\vec{E}_t = E_{t,x}\hat{x} + E_{t,y}\hat{y}$ for the same transmitter t is measured at points located on a measurement surface $\mathcal{S}$. The scattered electric field, defined by $\vec{E}_t^{\text{sct}} \triangleq \vec{E}_t - \vec{E}_t^{\text{inc}}$, satisfies the vector wave equation

$$\nabla \times \nabla \times \vec{E}_t^{\text{sct}}(\boldsymbol{r}) - k_b^2(\boldsymbol{r})\, \vec{E}_t^{\text{sct}}(\boldsymbol{r}) = k_b^2(\boldsymbol{r})\, \vec{w}_t(\boldsymbol{r}) \qquad (1)$$

where $k_b(\boldsymbol{r}) = \omega\sqrt{\mu_0\epsilon_0\epsilon_b(\boldsymbol{r})}$ is the background wave-number, and $\vec{w}_t(\boldsymbol{r}) \triangleq \chi(\boldsymbol{r})\, \vec{E}_t(\boldsymbol{r})$ is the contrast source.

Solving the partial differential equation (PDE) for the scattered field vector, $\vec{E}_t^{\text{sct}}$, requires the boundary conditions (BCs) on Γ be defined. For a conductive-enclosure system a perfect electrical conductor (PEC) boundary condition is used resulting in a homogeneous Dirichlet BC:

$$\hat{n} \times \vec{E}_t^{\text{sct}}(\boldsymbol{r}) = 0 \quad \text{for} \quad \boldsymbol{r} \in \Gamma \qquad (2)$$

where $\hat{n}$ denotes the outward-normal unit vector on the boundary Γ.

For unbounded-region problems, the field at the boundary of the problem is required to satisfy the 2D Sommerfeld boundary condition:

$$\lim_{r\to\infty} r\Big(\nabla \times \vec{E}_t^{\text{sct}}(\boldsymbol{r}) + jk_b\hat{r} \times \vec{E}_t^{\text{sct}}(\boldsymbol{r})\Big) = 0, \qquad (3)$$

where the radial coordinate $r = \sqrt{x^2 + y^2}$ and the radial unit vector $\hat{r} = \boldsymbol{r}/r$.

III. THE FINITE-ELEMENT METHOD

The boundary-value problem (BVP) defined by the second order PDE, (1), and the boundary conditions is solved using FEM with the Rayleigh-Ritz variational method [38]. The problem domain, Ω, is divided into a mesh of M triangular elements characterized by N nodes that are interconnected by a total number of E edges. Each edge is associated with linear vector basis functions (also known as Whitney elements [32]) whose parameters are dependent on the geometry of the mesh. Utilizing the Rayleigh-Ritz method to solve (1) produces the FEM matrix equation

$$\boldsymbol{\mathcal{K}}_b\, \big[\underline{E}_{t,\Omega}^{\text{sct}}\big] = \vec{\boldsymbol{\mathcal{R}}}_b \cdot \underline{\vec{w}}_{t,\Omega}. \qquad (4)$$

Here $\boldsymbol{\mathcal{K}}_b \in \mathbb{C}^{E\times E}$ is the FEM discretization matrix which depends on the BCs and the background medium properties, and $\vec{\boldsymbol{\mathcal{R}}}_b \in \mathbb{C}^{E\times M}$ is a "mass" matrix which depends on the background medium properties. Each entry of $\vec{\boldsymbol{\mathcal{R}}}_b$ is a vector with x- and y-components, thus $\vec{\boldsymbol{\mathcal{R}}}_b = \boldsymbol{\mathcal{R}}_{b,x}\, \hat{x} + \boldsymbol{\mathcal{R}}_{b,y}\, \hat{y}$. The data vector $\underline{E}_{t,\Omega}^{\text{sct}} \in \mathbb{C}^E$ contains the scattered field values along the edges of the mesh, while $\underline{\vec{w}}_{t,\Omega} \in \mathbb{C}^M$ is a column vector that holds the contrast source spatial-vector fields located at the centroids of the triangles in Ω. For triangles outside the imaging domain, $\mathcal{D}$, their corresponding values in $\underline{\vec{w}}_{t,\Omega}$ are equal to zero.

Regardless of the BC type, the entry at the i^{th} row and j^{th} column of the matrix $\boldsymbol{\mathcal{K}}_b$ is given by

$$\boldsymbol{\mathcal{K}}_{b_{i,j}} = \int_\Omega \big(\nabla \times \vec{N}_i(\boldsymbol{r})\big) \cdot \big(\nabla \times \vec{N}_j(\boldsymbol{r})\big) - k_b^2(\boldsymbol{r})\, \vec{N}_i(\boldsymbol{r}) \cdot \vec{N}_j(\boldsymbol{r})\, dv \qquad (5)$$

where $\vec{N}_i$ and $\vec{N}_j$ are the linear vector basis functions defined at the i^{th} and j^{th} edge respectively.

For unbounded problems the Sommerfeld BC is modeled using a first-order absorbing BC [38]. This leads to a boundary integral term that contributes to the $(i,\ i)$th element of $\boldsymbol{\mathcal{K}}_b$ as

$$\boldsymbol{\mathcal{K}}_{b_{i,i}}^{\Gamma} = \int_\Gamma j\, k_b(\boldsymbol{r})\, \big(\hat{n} \times \vec{N}_i(\boldsymbol{r})\big) \cdot \big(\hat{n} \times \vec{N}_i(\boldsymbol{r})\big)\, ds \qquad (6)$$

where i is the global index of a triangle edge along the problem boundary. For problems with conductive enclosures, the homogeneous Dirichlet boundary conditions are enforced as the matrix $\boldsymbol{\mathcal{K}}_b$ is built.

The entry at the i^{th} row and k^{th} column of the matrix $\vec{\boldsymbol{\mathcal{R}}}_b$ is calculated as

$$\vec{\boldsymbol{\mathcal{R}}}_{b_{i,k}} = \int_{\Omega_k} k_{b,k}^2\, \vec{N}_i(\boldsymbol{r})\, dv \qquad (7)$$

where $\vec{N}_i$ is a Whitney element defined at edge i belonging to the k^{th} triangle, while Ω_k and $k_{b,k}$ are, respectively, the domain covered by and the wave-number assigned to the k^{th} triangle.

The inversion algorithm can be more effectively implemented and described by defining several matrix operators. The first operator, $\vec{\boldsymbol{\mathcal{M}}}_{\mathcal{S}} \in \mathbb{C}^{R\times E}$, is a matrix that transforms field values along E edges of the problem domain Ω to the R receiver locations on the measurement surface $\mathcal{S}$. The result of the transformation are field vectors with x- and y- components.

The second operator, $\vec{\boldsymbol{\mathcal{M}}}_{\mathcal{D}} \in \mathbb{R}^{I\times E}$, is a matrix that transforms field values along E edges of the problem domain Ω to the I contrast source variables located in the imaging domain $\mathcal{D}$. Each element of the resulting transformation is located at a triangle centroid and it consists of a field vector with x- and y- components.

Both of these matrices are interpolatory operators that calculate the spatial-vector field values at either the location on the measurement surface $\mathcal{S}$ or the imaging domain $\mathcal{D}$ using the FEM vector basis functions.

The inverse FEM matrix operator, denoted as $\vec{\boldsymbol{\mathcal{L}}} \in \mathbb{C}^{E\times I}$, returns the scattered field values $\underline{E}_{t,\Omega}^{\text{sct}}$ along the E mesh edges given a column vector of the contrast source spatial-vector values, $\underline{\vec{w}}_t \in \mathbb{C}^I$, at the I triangle centroids inside the imaging domain. It is written as

$$\underline{E}_{t,\Omega}^{\text{sct}} = \vec{\boldsymbol{\mathcal{L}}}[\underline{\vec{w}}_t] = \boldsymbol{\mathcal{K}}_b^{-1}\vec{\boldsymbol{\mathcal{R}}}_b \cdot \boldsymbol{\mathcal{M}}_U^T[\underline{\vec{w}}_t] \qquad (8)$$

where $\boldsymbol{\mathcal{M}}_U \in \mathbb{R}^{I\times M}$ is a selection matrix that returns centroid values for only the triangles located in the imaging domain, $\mathcal{D}$, given centroid values for all the M elements in Ω.

The matrices obtained using FEM are sparse and symmetric, thus for 2D problems $\underline{E}_{t,\Omega}^{\text{sct}}$ can be computed efficiently using

LU-decomposition for sparse matrices. Moreover, these matrices are independent of the OI and the location of the transmitter t, so they can be assembled once, stored, and recalled when necessary.

IV. INVERSION ALGORITHM

The overall objective of the CSI algorithm is to update the contrast source, $\underline{\vec{w}}_t$, and the contrast, $\underline{\chi}$, variables sequentially so as to minimize the functional

$$\mathcal{F}^{\mathrm{CSI}}(\underline{\chi}, \underline{\vec{w}}_t) = \mathcal{F}^{\mathcal{S}}(\underline{\vec{w}}_t) + \mathcal{F}^{\mathcal{D}}(\underline{\chi}, \underline{\vec{w}}_t) \tag{9}$$

where the data-error equation $\mathcal{F}^{\mathcal{S}}(\underline{\vec{w}}_t)$ and the domain-error equation $\mathcal{F}^{\mathcal{D}}(\underline{\chi}, \underline{\vec{w}}_t)$ are given by

$$\begin{aligned} \mathcal{F}^{\mathcal{S}}(\underline{\vec{w}}_t) &= \frac{\sum_t \left\| \underline{\vec{u}}_t - \vec{\boldsymbol{\mathcal{M}}}_{\mathcal{S}} \vec{\boldsymbol{\mathcal{L}}}[\underline{\vec{w}}_t] \right\|_{\mathcal{S}}^2}{\sum_t \|\underline{\vec{u}}_t\|_{\mathcal{S}}^2} \\ \mathcal{F}^{\mathcal{D}}(\underline{\chi}, \underline{\vec{w}}_t) &= \frac{\sum_t \left\| \underline{\chi} \odot \underline{\vec{E}}_t^{\mathrm{inc}} - \underline{\vec{w}}_t + \underline{\chi} \odot \vec{\boldsymbol{\mathcal{M}}}_{\mathcal{D}} \vec{\boldsymbol{\mathcal{L}}}[\underline{\vec{w}}_t] \right\|_{\mathcal{D}}^2}{\sum_t \left\| \underline{\chi} \odot \underline{\vec{E}}_t^{\mathrm{inc}} \right\|_{\mathcal{D}}^2}. \end{aligned} \tag{10}$$

For a transmitter t, $\underline{\vec{u}}_t \in \mathbb{C}^R$ is a vector of the measured scattered field at R receiver locations per transmitter, $\underline{\chi} \in \mathbb{C}^I$ corresponds to a vector of the contrast values located at the triangle centroids of $\mathcal{D}$ and $\underline{\vec{E}}_t^{\mathrm{inc}} \in \mathbb{C}^I$ holds the incident field vector values at the triangle centroids in $\mathcal{D}$.

For R points equally distributed on a measurement surface $\mathcal{S}$, the inner product in $\mathcal{F}^{\mathcal{S}}(\underline{\vec{w}}_t)$ is defined as

$$\|\underline{\vec{a}}\|_{\mathcal{S}}^2 = \underline{a}_x^H \underline{a}_x + \underline{a}_y^H \underline{a}_y \tag{11}$$

where $\underline{a}_x$ and $\underline{a}_y$ are the x- and y- components of an arbitrary vector $\underline{\vec{a}} \in \mathbb{C}^R$, and the superscript H denotes the Hermitian operator (complex-conjugate transpose). Similarly, for I points located at the triangle centroids of the imaging domain $\mathcal{D}$, the inner product in $\mathcal{F}^{\mathcal{D}}(\underline{\chi}, \underline{\vec{w}}_t)$ is calculated as

$$\left\| \underline{\vec{b}} \right\|_{\mathcal{D}}^2 = \underline{b}_x^H \boldsymbol{\mathcal{T}}_{\mathcal{D}} \underline{b}_x + \underline{b}_y^H \boldsymbol{\mathcal{T}}_{\mathcal{D}} \underline{b}_y \tag{12}$$

where $\underline{b}_x$ and $\underline{b}_y$ are the x- and y- components of an arbitrary vector $\underline{\vec{b}} \in \mathbb{C}^I$ and $\boldsymbol{\mathcal{T}}_{\mathcal{D}} \in \mathbb{R}^{I \times I}$ is a diagonal matrix whose entities are the areas of the triangles inside $\mathcal{D}$.

The first step in CSI is to update the contrast source variables $\underline{\vec{w}}_t$ by a conjugate-gradient (CG) method with Polak-Ribière search directions; here the contrast variables, $\underline{\chi}$, are held constant. The next step is updating the contrast variables, $\underline{\chi}$, analytically by minimizing the domain-error functional, $\mathcal{F}^{\mathcal{D}}(\underline{\chi}, \underline{\vec{w}}_t)$, with respect to $\underline{\chi}$; the contrast source variables, $\underline{\vec{w}}_t$, are assumed constant in this step. The details of the algorithm formulation for 2D TE problems within the framework of FEM are detailed in the appendix.

A. Multiplicatively Regularized CSI

The weighted L_2-norm total variation multiplicative regularization (MR) has been incorporated into various inversion algorithms including CSI [39], [40]. The addition of the multiplicative regularization term enhances the outcome of the inversion algorithm and improves the algorithm performance with noisy measurement data.

With the MR term, the CSI functional becomes

$$\mathcal{F}_n(\underline{\chi}, \underline{\vec{w}}_t) = \mathcal{F}_n^{\mathrm{MR}}(\underline{\chi}) \times \mathcal{F}^{\mathrm{CSI}}(\underline{\chi}, \underline{\vec{w}}_t) \tag{13}$$

where the regularization term $\mathcal{F}_n^{\mathrm{MR}}(\underline{\chi})$ is given by

$$\mathcal{F}_n^{\mathrm{MR}}(\underline{\chi}) = \int_{\mathcal{D}} \underline{b}_n^2 \left(|\nabla \underline{\chi}|^2 + \delta_n^2 \right) d\boldsymbol{r}. \tag{14}$$

Here

$$\begin{aligned} \underline{b}_n &= \sqrt{\left(A \left(|\nabla \underline{\chi}_{n-1}|^2 + \delta_n^2 \right) \right)^{-1}} \\ \delta_n^2 &= \mathcal{F}^{\mathcal{D}}(\underline{\chi}_n^{\mathrm{CSI}}, \underline{\vec{w}}_{t,n})\, \bar{A}^{-1} \end{aligned} \tag{15}$$

where A is the total area of domain $\mathcal{D}$ and $\bar{A}$ is the mean area of the triangles in the imaging domain $\mathcal{D}$.

Since $\mathcal{F}^{\mathrm{MR}}(\underline{\chi}_{n-1}) = 1$, the update procedure for the contrast source variables, $\underline{\vec{w}}_t$, remains unchanged. For the contrast variables, $\underline{\chi}$, they are first evaluated using (25), then the results are updated by a CG method with Polak-Ribère search directions as outlined in [39], [41]. The details for incorporating the multiplicative regularization term to FEM-CSI can be found in [10].

V. INVERSION RESULTS

In this section, the MR-FEM-CSI algorithm for 2D TE problems is tested using the Fresnel experimental datasets as well as synthetically generated data. An inverse crime is avoided when using the synthetically generated datasets by adding 5% white noise to the scattered field data [42]. In addition, different meshes are used to generate the synthetic data than the ones used to perform the inversion. During the inversion process, the estimates at each iteration are constrained to lie within physical bounds, that is $\mathrm{Re}(\epsilon_r) \geq 1$ and $\mathrm{Im}(\epsilon_r) \leq 0$. For each example, the inversion algorithm is run for 2048 iterations to ensure convergence.

A summary of each example is provided in Table I where the frequencies (f), the number of transmitters per frequency (T), the number of triangles in the problem domain Ω (M), the number of triangles in the imaging domain $\mathcal{D}$ (I), the average time per iteration (t_{iter}) and the logarithm of the data-error function $\mathcal{F}^{\mathcal{S}}$ after the last iteration are specified. For synthetic datasets, the relative L_2-norm of the difference between the actual profile and the reconstruction is specified [9]. The memory requirement (in megabytes, MB) as well as the computational time (t_{LU}) for LU-decomposition are also given in the table; LU-decomposition is performed once for each run of the inversion algorithm, then saved and recalled when necessary. The inversion algorithm is implemented in MATLAB and was run on a PC workstation with two Intel Xeon quad-core 2.8 GHz processors.

TABLE I
SUMMARY OF INVERSION EXAMPLES

Example	f (GHz)	T	M	I	t_{iter} (seconds)	$\log(\mathcal{F}^{S})$	L_2	LU-decomposition Memory (MB)	LU-decomposition t_{LU} (seconds)
Fresnel Experimental Datasets			40982	17887				56	0.84
FoamDielExt.	2 - 10	8			21	-4.11			
FoamDielInt.	2 - 10	8			21	-4.06			
FoamTwinDiel.	2 - 10	18			30	-4.07			
FoamMetExt.	2 - 18	18			75				
Circular Lossy Targets	1	32							
Triangular Conductive Enclosure			40159	12238	9	-5.00	18.23%	48	0.75
Unbounded			24338	12375	6	-5.25	18.35%	30	0.45

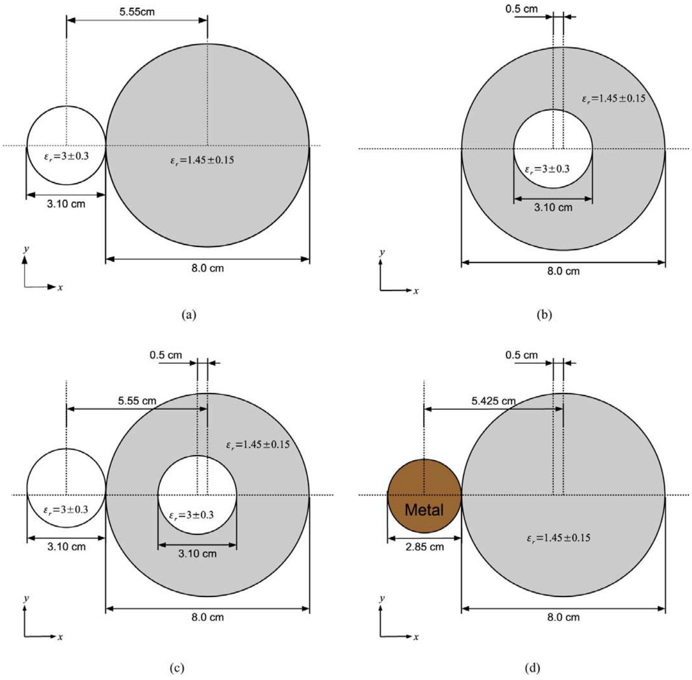

(a) (b) (c) (d)

Fig. 1. The targets of the Fresnel data set (a) *FoamDielExt.* (b) *FoamDielInt.* (c) *FoamTwinDiel.* (d) *FoamMetExt.*.

A. Fresnel Institute Datasets

The first examples focus on inverting multi-frequency experimental datasets collected by the Fresnel Institute in 2005 for different inhomogeneous targets depicted in Fig. 1: *FoamDieExt.*, *FoamDielInt.*, *FoamTwinDiel.* and *FoamMetExt.*[43]. In these datasets, the transmitting and receiving antennas are both wideband horn antennas located on a circle having a 1.67 m radius. The targets are all circular cylinders with no variation in the longitudinal z-direction. For all the targets, the background medium is free-space with $\epsilon_b = 1$. For the TE illumination, the ϕ-component of the scattered field is measured and calibrated, then converted to the x- and y- components to be used by the inversion algorithm.

The *FoamDielExt.* and *FoamDielInt.* targets are interrogated by 8 transmitters and the measured data is collected at 9 different frequencies from 2 GHz to 10 GHz with a step of 1 GHz at 241 receiver points per transmitter. The *FoamTwinDiel.* target is illuminated by 18 transmitters and the number of frequencies and receivers is the same as the previous two targets. As for the *FoamMetExt.* target, while the number of transmitters and receivers is the same as in the *FoamTwinDiel.* datasets, the object is irradiated at 17 different frequencies in the range from 2 GHz to 18 GHz with 1 GHz step.

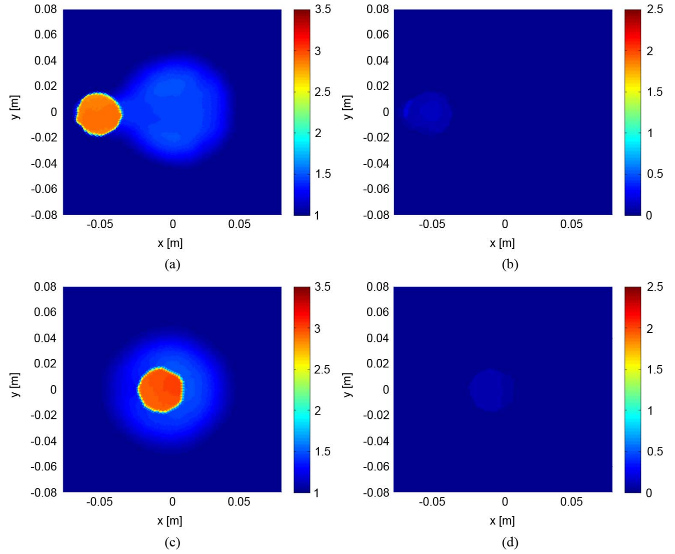

(a) (b) (c) (d)

Fig. 2. The reconstruction of (a)-(b) *FoamDielExt.* and (c)–(d) *FoamDielInt.* datasets. The real part of the reconstructions $\mathrm{Re}(\epsilon_r)$ are presented in the left-column, while the imaginary parts $-\mathrm{Im}(\epsilon_r)$ are shown in the right-column.

The data for the different frequencies are inverted simultaneously using the MR-FEM-CSI algorithm presented herein. The extension to the algorithm allowing it to deal simultaneously with multi-frequency datasets, for a lossless background, is trivial. Some of the details of this extension can be found in [8], [27]. The inversion domain $\mathcal{D}$ is a square region centered in the problem domain Ω with the side length equal to 15 cm. The unknown variables are located at the centroids of 17,887 triangles.

The reconstruction results for the different datasets are shown in Figs. 2 and 3. The foam cylinder with diameter 8 cm is reconstructed well for all the datasets with an average relative permittivity of $\epsilon_r^{\text{reconstr}} \approx 1.4$. For the *FoamDielExt.*, *FoamDielInt.* and *FoamTwinDiel.* datasets, the location and the shape of the plastic cylinders with diameter 3.1 cm are estimated correctly. The average relative permittivity for the plastic cylinder reconstructions is $\epsilon_r^{\text{reconstr}} \approx 2.9 - j0.11$, although the object is lossless. The artifacts in the imaginary part are consistent with

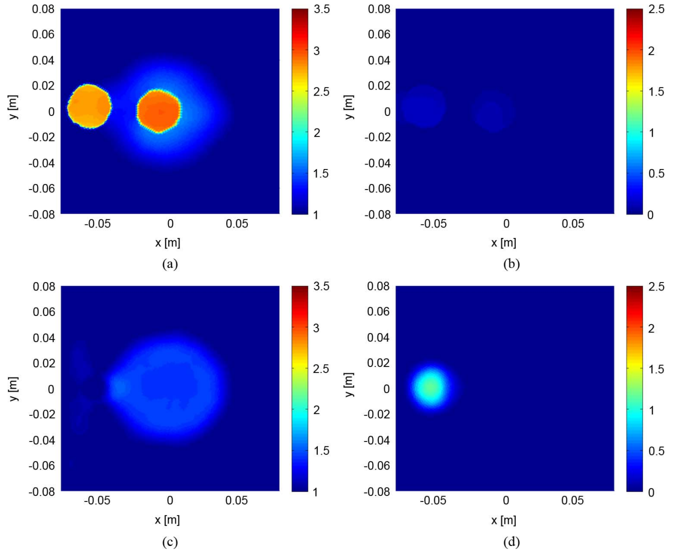

Fig. 3. The reconstruction of (a)–(b) *FoamTwinDiel.* and (c)–(d) *FoamMetExt.* datasets. The real part of the reconstructions $\mathrm{Re}(\epsilon_r)$ are presented in the left-column, while the imaginary parts $-\mathrm{Im}(\epsilon_r)$ are shown in the right-column.

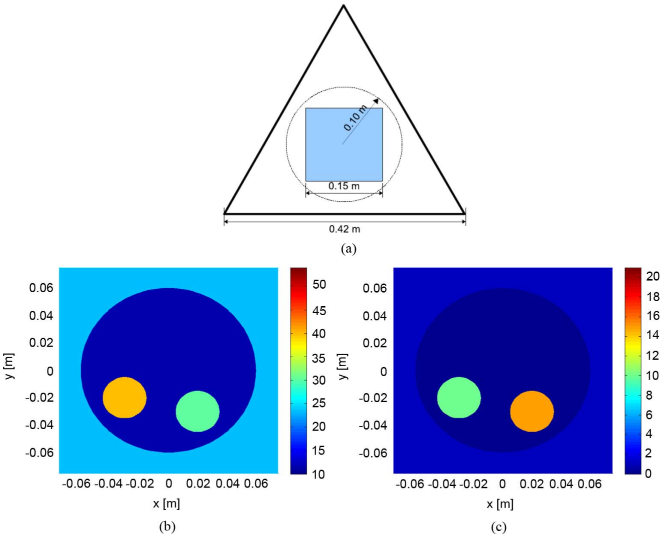

Fig. 4. (a) Triangular conductive enclosure configuration, along with (b) the real $\mathrm{Re}(\epsilon_r)$ and (c) the imaginary $-\mathrm{Im}(\epsilon_r)$ exact profile of the OI with a low-loss background at a frequency $f = 1$ GHz.

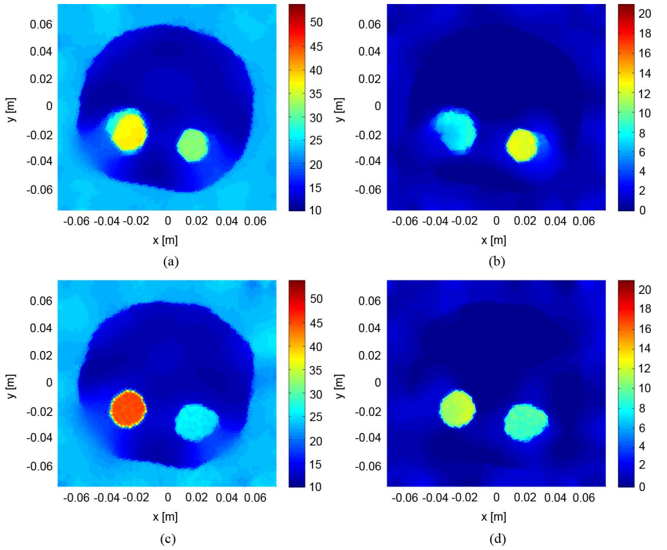

Fig. 5. The MR-FEMCSI reconstructions at a frequency $f = 1$ GHz (a)-(b) for an unbounded domain problem and (c)-(d) for a domain enclosed by triangular conductive boundary. The real part of the reconstructions $\mathrm{Re}(\epsilon_r)$ are presented in the left-column, while the imaginary parts $-\mathrm{Im}(\epsilon_r)$ are shown in the right-column.

the results obtained using the Gauss-Newton inversion algorithm [7]. For the *FoamMetExt.* dataset reconstruction, theoretically the inversion should only obtain the boundary of the metallic cylinder; the contrast sources inside the cylinder are invisible. The inversion algorithm constructed the real part of the metallic cylinder to a value close to 1, whereas the reconstructed value of the imaginary part is ≈ -1.45 indicating an object with loss. As for the location of the metallic cylinder it is estimated correctly relative to the foam cylinder position. The results achieved using simultaneous frequency inversion of the TE data using our MR-FEM-CSI algorithm are quite similar to those obtained using IE-MR-CSI [8].

B. Imaging Inside a Conductive Enclosure

As previously discussed, one advantage of using an FEM-based inversion algorithm is the ability to perform imaging in different conductive enclosure shapes without any modifications to the algorithm itself [9], [44]. In this section, microwave imaging for the TE case is done in a triangular conductive enclosure.

The object-of-interest consists of three circular regions with electrical properties that resemble biological tissues. One of the circular regions has a radius of 6 cm with a relative permittivity of $\epsilon_r = 12$. In this region, the other two circular regions are embedded. The two regions have the same radius of 1.5 cm with complex relative permittivities of $\epsilon_r = 40 - j10$ and $\epsilon_r = 30 - j15$ at a frequency of $f = 1$ GHz. The target configuration is shown in Fig. 4.

The OI is centered within a conductive enclosure shaped as an equilateral triangle of side length equal to 42 cm, and it is surrounded by a background medium of relative permittivity $\epsilon_b = 23.4 - j1.13$ at a frequency $f = 1$ GHz. The OI is interrogated by 32 transmitters and the scattered data are collected at 32 receivers per transmitter. The transmitters are magnetic line sources. The scattered field data collected is along both the x and y directions in the TE case. The transmitting and receiving points are evenly spaced on a circle of radius 10 cm. For comparison purposes, imaging is performed also with the OI immersed in an unbounded homogeneous region.

The inversion domain $\mathcal{D}$ is a square centered in the middle of the problem domain with side length equal to 15 cm. The inversion domain consists of approximately 12,000 unstructured arbitrarily oriented triangles. The unknown contrast, $\underline{\chi}$, and contrast source, $\underline{\vec{w}}_t$, variables in the inversion algorithm are located at the centroids of these triangles.

The reconstructions after 2048 iterations are shown in Fig. 5. For both configurations, the unbounded and the triangular conductive enclosure, the features of the OI are reconstructed successfully. The complex relative permittivity of the left inner circular region is estimated more accurately for imaging inside the conductive enclosure than its unbounded domain counterpart; inside the conductive enclosure the average reconstructed permittivity is $\epsilon_r^{\text{reconstr}} \approx 43 - j9$, whereas in the unbounded problem $\epsilon_r^{\text{reconstr}} \approx 31 - j6$. As for the right circular region, the reconstructed complex permittivity is underestimated for imaging in both configurations; the average reconstructed permittivity is $\epsilon_r^{\text{reconstr}} \approx 23 - j8$ for imaging inside the conductive chamber and $\epsilon_r^{\text{reconstr}} \approx 24 - j12$ for the unbounded problem. The average relative permittivity for the circle with radius 6 cm is approximately 13 for both imaging setups.

VI. CONCLUSION

A multiplicatively regularized finite-element method contrast source inversion (MR-FEM-CSI) algorithm has been presented and validated for 2D microwave imaging under the TE approximation of the fields. The algorithm retains the advantages of FEM-CSI, such as the ability to invert on an unstructured triangular mesh, as well as the ease of modeling different boundary types and shapes. Unlike the TM case, for TE electromagnetic problems edge-based elements with linear vector basis functions are used as they are superior to node-based elements when solving vectorial problems. The use of an edge-based FEM with the inversion algorithm requires the implementation of several non-trivial operators to transform between field values along mesh edges and the unknown variables located at the triangle centroids.

The performance of the algorithm is demonstrated by inverting the Fresnel Institute TE experimental datasets, as well as synthetic datasets.

APPENDIX

With the contrast variables, $\underline{\chi}$, held constant, the first step in CSI is to update the contrast source variables $\underline{\vec{w}}_t$ by a conjugate-gradient (CG) method with Polak-Ribière search directions $\underline{\vec{d}}_t$ as follows:

$$\underline{\vec{w}}_{t,n} = \underline{\vec{w}}_{t,n-1} + \alpha_{t,n}\underline{\vec{d}}_{t,n} \tag{16}$$

where subscript n is the iteration number and $\alpha_{t,n}$ is the update step-size. A closed-form expression for $\alpha_{t,n}$ can be determined by solving the minimization

$$\alpha_{t,n} = \arg\,\min_\alpha \left\{\mathcal{F}^{\underline{\chi}_{n-1},\,\text{CSI}}\left(\underline{\vec{w}}_{t,n-1} + \alpha\,\underline{\vec{d}}_{t,n}\right)\right\}. \tag{17}$$

for α analytically. The search directions $\underline{\vec{d}}_{t,n}$ are evaluated as

$$\underline{\vec{d}}_{t,n} = -\underline{\vec{g}}_{t,n} + \frac{\left\langle \underline{\vec{g}}_{t,n}, \underline{\vec{g}}_{t,n} - \underline{\vec{g}}_{t,n-1}\right\rangle_\mathcal{D}}{\left\|\underline{\vec{g}}_{t,n-1}\right\|_\mathcal{D}^2}\underline{\vec{d}}_{t,n-1} \tag{18}$$

where $\underline{\vec{g}}_{t,n}$ is the gradient of the objective functional $\mathcal{F}^{\text{CSI}}(\underline{\chi}, \underline{\vec{w}}_t)$ with respect to the contrast source variables $\underline{\vec{w}}_t$ and is given by

$$\underline{\vec{g}}_{t,n} = \bar{\bar{\boldsymbol{\mathcal{G}}}}_\mathcal{S} \cdot \underline{\vec{\rho}}_{t,n-1} + \bar{\bar{\boldsymbol{\mathcal{G}}}}_\mathcal{D} \cdot \underline{\vec{r}}_{t,n-1}. \tag{19}$$

Here

$$\begin{aligned}\bar{\bar{\boldsymbol{\mathcal{G}}}}_\mathcal{S} &= \boldsymbol{\mathcal{G}}_{\mathcal{S},xx}\hat{x}\hat{x} + \boldsymbol{\mathcal{G}}_{\mathcal{S},yx}\hat{y}\hat{x} + \boldsymbol{\mathcal{G}}_{\mathcal{S},xy}\hat{x}\hat{y} + \boldsymbol{\mathcal{G}}_{\mathcal{S},yy}\hat{y}\hat{y}\\ \bar{\bar{\boldsymbol{\mathcal{G}}}}_\mathcal{D} &= \boldsymbol{\mathcal{G}}_{\mathcal{D},xx}\hat{x}\hat{x} + \boldsymbol{\mathcal{G}}_{\mathcal{D},yx}\hat{y}\hat{x} + \boldsymbol{\mathcal{G}}_{\mathcal{D},xy}\hat{x}\hat{y} + \boldsymbol{\mathcal{G}}_{\mathcal{D},yy}\hat{y}\hat{y}\end{aligned} \tag{20}$$

where each term is given by

$$\begin{aligned}\boldsymbol{\mathcal{G}}_{\mathcal{S},xx} &= -2\eta_\mathcal{S}\boldsymbol{\mathcal{T}}_\mathcal{D}^{-1}\boldsymbol{\mathcal{L}}_x^H\boldsymbol{\mathcal{M}}_{\mathcal{S},x}^H\\ \boldsymbol{\mathcal{G}}_{\mathcal{S},xy} &= -2\eta_\mathcal{S}\boldsymbol{\mathcal{T}}_\mathcal{D}^{-1}\boldsymbol{\mathcal{L}}_x^H\boldsymbol{\mathcal{M}}_{\mathcal{S},y}^H\\ \boldsymbol{\mathcal{G}}_{\mathcal{S},yx} &= -2\eta_\mathcal{S}\boldsymbol{\mathcal{T}}_\mathcal{D}^{-1}\boldsymbol{\mathcal{L}}_y^H\boldsymbol{\mathcal{M}}_{\mathcal{S},x}^H\\ \boldsymbol{\mathcal{G}}_{\mathcal{S},yy} &= -2\eta_\mathcal{S}\boldsymbol{\mathcal{T}}_\mathcal{D}^{-1}\boldsymbol{\mathcal{L}}_y^H\boldsymbol{\mathcal{M}}_{\mathcal{S},y}^H,\end{aligned} \tag{21}$$

and

$$\begin{aligned}\boldsymbol{\mathcal{G}}_{\mathcal{D},xx} &= -2\eta_{\mathcal{D},n-1}\boldsymbol{\mathcal{T}}_\mathcal{D}^{-1}\left(\boldsymbol{\mathcal{I}} - \boldsymbol{\mathcal{L}}_x^H\boldsymbol{\mathcal{M}}_{\mathcal{D},x}^H\boldsymbol{\mathcal{X}}_{n-1}^H\right)\boldsymbol{\mathcal{T}}_\mathcal{D}\\ \boldsymbol{\mathcal{G}}_{\mathcal{D},xy} &= 2\eta_{\mathcal{D},n-1}\boldsymbol{\mathcal{T}}_\mathcal{D}^{-1}\boldsymbol{\mathcal{L}}_x^H\boldsymbol{\mathcal{M}}_{\mathcal{D},y}^H\boldsymbol{\mathcal{X}}_{n-1}^H\boldsymbol{\mathcal{T}}_\mathcal{D}\\ \boldsymbol{\mathcal{G}}_{\mathcal{D},yx} &= 2\eta_{\mathcal{D},n-1}\boldsymbol{\mathcal{T}}_\mathcal{D}^{-1}\boldsymbol{\mathcal{L}}_y^H\boldsymbol{\mathcal{M}}_{\mathcal{D},x}^H\boldsymbol{\mathcal{X}}_{n-1}^H\boldsymbol{\mathcal{T}}_\mathcal{D}\\ \boldsymbol{\mathcal{G}}_{\mathcal{D},yy} &= -2\eta_{\mathcal{D},n-1}\boldsymbol{\mathcal{T}}_\mathcal{D}^{-1}\left(\boldsymbol{\mathcal{I}} - \boldsymbol{\mathcal{L}}_y^H\boldsymbol{\mathcal{M}}_{\mathcal{D},y}^H\boldsymbol{\mathcal{X}}_{n-1}^H\right)\boldsymbol{\mathcal{T}}_\mathcal{D}.\end{aligned} \tag{22}$$

Here $\boldsymbol{\mathcal{I}} \in \mathbb{R}^{I\times I}$ is an identity matrix and $\boldsymbol{\mathcal{X}}_{n-1} = \text{diag}(\underline{\chi}_{n-1})$ is a diagonal matrix. The normalization terms $\eta_\mathcal{S}$ and $\eta_{\mathcal{D},n-1}$ are given by

$$\begin{aligned}\eta_\mathcal{S} &= \left(\sum_t \|\underline{\vec{u}}_t\|_\mathcal{S}^2\right)^{-1},\\ \eta_{\mathcal{D},n-1} &= \left(\sum_t \left\|\underline{\chi}_{n-1}\odot\underline{\vec{E}}_t^{\text{inc}}\right\|_\mathcal{D}^2\right)^{-1},\end{aligned} \tag{23}$$

while the error terms $\underline{\vec{\rho}}_{t,n-1}$ and $\underline{\vec{r}}_{t,n-1}$ in (19) are calculated as

$$\begin{aligned}\underline{\vec{\rho}}_{t,n-1} &= \underline{\vec{u}}_t - \vec{\boldsymbol{\mathcal{M}}}_\mathcal{S}\vec{\boldsymbol{\mathcal{L}}}[\underline{\vec{w}}_{t,n-1}],\\ \underline{\vec{r}}_{t,n-1} &= \underline{\chi}_{n-1}\odot\underline{\vec{E}}_t^{\text{inc}} - \underline{\vec{w}}_{t,n-1}\\ &\quad + \underline{\chi}_{n-1}\odot\vec{\boldsymbol{\mathcal{M}}}_\mathcal{D}\vec{\boldsymbol{\mathcal{L}}}[\underline{\vec{w}}_{t,n-1}].\end{aligned} \tag{24}$$

The matrices $\boldsymbol{\mathcal{M}}_{\mathcal{S},x}$ and $\boldsymbol{\mathcal{M}}_{\mathcal{D},x}$ contain the x-components of matrices $\vec{\boldsymbol{\mathcal{M}}}_\mathcal{S}$ and $\vec{\boldsymbol{\mathcal{M}}}_\mathcal{D}$ entries; likewise, matrices $\boldsymbol{\mathcal{M}}_{\mathcal{S},y}$ and $\boldsymbol{\mathcal{M}}_{\mathcal{D},y}$ hold the y-components. As for matrices $\boldsymbol{\mathcal{L}}_x$ and $\boldsymbol{\mathcal{L}}_y$, they can be written as

$$\boldsymbol{\mathcal{L}}_x = \boldsymbol{\mathcal{K}}_b^{-1}\boldsymbol{\mathcal{R}}_{b,x}\boldsymbol{\mathcal{M}}_U^T \quad\text{and}\quad \boldsymbol{\mathcal{L}}_y = \boldsymbol{\mathcal{K}}_b^{-1}\boldsymbol{\mathcal{R}}_{b,y}\boldsymbol{\mathcal{M}}_U^T.$$

The next step in CSI is updating the contrast variables, $\underline{\chi}$, while the contrast source variables, $\underline{\vec{w}}_t$, are assumed constant. This requires minimizing the domain-error functional, $\mathcal{F}^\mathcal{D}(\underline{\chi}, \underline{\vec{w}}_t)$, with respect to $\underline{\chi}$ while assuming the normalization term $\eta_\mathcal{D}$ constant. The minimizer at the n^{th} iteration is the solution for the following sparse matrix equation for $\underline{\chi}_n$:

$$\left(\sum_t \vec{\boldsymbol{\mathcal{E}}}_{t,n}^H \cdot \boldsymbol{\mathcal{T}}_\mathcal{D}\vec{\boldsymbol{\mathcal{E}}}_{t,n}\right)\underline{\chi}_n = \sum_t \vec{\boldsymbol{\mathcal{E}}}_{t,n}^H \cdot \boldsymbol{\mathcal{T}}_\mathcal{D}\underline{\vec{w}}_{t,n}. \tag{25}$$

Here $\vec{\boldsymbol{\mathcal{E}}}_{t,n} \in \mathbb{C}^{I\times I}$ is the total field diagonal matrix where the diagonal entries are the elements of the vector $\underline{\vec{E}}_{t,n} = \underline{\vec{E}}_t^{\text{inc}} + \vec{\boldsymbol{\mathcal{M}}}_\mathcal{D}\vec{\boldsymbol{\mathcal{L}}}[\underline{\vec{w}}_{t,n}]$.

The initial guess for the FEM-CSI algorithm, $\underline{\vec{w}}_{t,0}$, is not set to zero, but rather is taken to be the minimizer of the data-error functional $\mathcal{F}^{\mathcal{S}}(\underline{\vec{w}}_t)$ after one line-minimization in the method of steepest descent. This initial guess is calculated as

$$\underline{\vec{w}}_{t,0} = \frac{\mathrm{Re}\left\langle \vec{\boldsymbol{\mathcal{M}}}_{\mathcal{S}}\vec{\boldsymbol{\mathcal{L}}}[\bar{\bar{\boldsymbol{\mathcal{G}}}}_{\mathcal{S}}\cdot\underline{\vec{u}}_t], \underline{\vec{u}}_t\right\rangle_{\mathcal{S}}}{\left\|\vec{\boldsymbol{\mathcal{M}}}_{\mathcal{S}}\vec{\boldsymbol{\mathcal{L}}}[\bar{\bar{\boldsymbol{\mathcal{G}}}}_{\mathcal{S}}\cdot\underline{\vec{u}}_t]\right\|^2_{\mathcal{S}}}\bar{\bar{\boldsymbol{\mathcal{G}}}}_{\mathcal{S}}\cdot\underline{\vec{u}}_t. \qquad (26)$$

After evaluating $\underline{\vec{w}}_{t,0}$, the initial guess for the contrast, $\underline{\chi}_0$, is calculated using (25). The initial search directions $\underline{\vec{d}}_{t,0}$ are set equal to zero.

ACKNOWLEDGMENT

The authors would like to thank the Institut Fresnel of Marseilles, France, for providing the experimental datasets.

REFERENCES

[1] T. Rubæk, T. K. P. Meaney, P. Meincke, and K. Paulsen, "Nonlinear microwave imaging for breast-cancer screening using Gauss-Newton's method and the CGLS inversion algorithm," *IEEE Trans. Antennas Propag.*, vol. 55, no. 8, pp. 2320–2331, 2007.

[2] P. Meaney, K. Paulsen, S. Geimer, S. Haider, and M. Fanning, "Quantification of 3-D field effects during 2-D microwave imaging," *IEEE Trans. Biomed. Eng.*, vol. 49, no. 7, pp. 708–720, 2002.

[3] C. Gilmore, P. Mojabi, A. Zakaria, M. Ostadrahimi, C. Kaye, S. Noghanian, L. Shafai, S. Pistorius, and J. LoVetri, "A wideband microwave tomography system with a novel frequency selection procedure," *IEEE Trans. Biomed. Eng.*, vol. 57, no. 4, pp. 894–904, Apr. 2010.

[4] P. M. Meaney, M. W. Fanning, T. Raynolds, C. J. Fox, Q. Fang, C. A. Kogel, S. P. Poplack, and K. D. Paulsen, "Initial clinical experience with microwave breast imaging in women with normal mammography," *Acad Radiol.*, Mar. 2007.

[5] S. Semenov, R. Svenson, A. Bulyshev, A. Souvorov, A. Nazarov, Y. Sizov, V. Posukh, A. Pavlovsky, P. Repin, and G. Tatsis, "Spatial resolution of microwave tomography for detection of myocardial ischemia and infarction-experimental study on two-dimensional models," *IEEE Trans. Microwave Theory Tech.*, vol. 48, no. 4, pp. 538–544, 2000.

[6] S. Y. Semenov and D. R. Corfield, "Microwave tomography for brain imaging: Feasibility assessment for stroke detection," *Int. J. Antennas Propag.*, vol. 2008, p. 8, 2008.

[7] P. Mojabi and J. LoVetri, "Comparison of TE and TM inversions in the framework of the Gauss-Newton method," *IEEE Trans. Antennas Propag.*, vol. 58, no. 4, pp. 1336–1348, 2010.

[8] A. Abubakar, P. M. van den Berg, and T. M. Habashy, "Application of the multiplicative regularized contrast source inversion method on TM- and TE-polarized experimental fresnel data," *Inverse Prob.*, vol. 21, pp. S5–S13, 2005.

[9] A. Zakaria, C. Gilmore, and J. LoVetri, "Finite-element contrast source inversion method for microwave imaging," *Inverse Prob.*, vol. 26, no. 11, p. 115010, 2010.

[10] A. Zakaria and J. LoVetri, "Application of multiplicative regularization to the finite-element contrast source inversion method," *IEEE Trans. Antennas Propag.*, vol. 59, no. 9, pp. 3495–3498, Sep. 2011.

[11] J. De Zaeytijd, A. Franchois, C. Eyraud, and J.-M. Geffrin, "Full-wave three-dimensional microwave imaging with a regularized Gauss-Newton method—Theory and experiment," *IEEE Trans. Antennas Propag.*, vol. 55, no. 11, pp. 3279–3292, 2007.

[12] S. Y. Semenov, R. H. Svenson, A. E. Bulyshev, A. E. Souvorov, A. G. Nazarov, Y. E. Sizov, V. G. Posukh, A. Pavlovsky, P. N. Repin, A. N. Starostin, B. A. Voinov, M. Taran, G. P. Tatsis, and V. Y. Baranov, "Three-dimensional microwave tomography: Initial experimental imaging of animals," *IEEE Trans. Biomed. Eng.*, vol. 49, no. 1, pp. 55–63, 2002.

[13] Q. Fang, P. M. Meaney, and K. D. Paulsen, "Viable three-dimensional medical microwave tomography: Theory and numerical experiments," *IEEE Trans. Antennas Propag.*, vol. 58, no. 2, pp. 449–458, 2010.

[14] B. Kooij and P. van den Berg, "Nonlinear inversion in TE scattering," *IEEE Trans. Microwave Theory Tech.*, vol. 46, no. 11, pp. 1704–1712, 1998.

[15] W. C. Chew and Y. M. Wang, "Reconstruction of two-dimensional permittivity distribution using the distorted born iterative method," *IEEE Trans. Med. Imaging*, vol. 9, no. 2, pp. 218–225, 1990.

[16] A. Abubakar, P. M. van den Berg, and S. Y. Semenov, "Two- and three-dimensional algorithms for microwave imaging and inverse scattering," *J. Electrom. Waves. Applicat.*, vol. 17, no. 2, pp. 209–231, 2003.

[17] C. Gilmore, P. Mojabi, and J. LoVetri, "Comparison of an enhanced distorted born iterative method and the multiplicative-regularized contrast source inversion method," *IEEE Trans. Antennas Propag.*, 2009.

[18] P. Mojabi and J. LoVetri, "Overview and classification of some regularization techniques for the Gauss-Newton inversion method applied to inverse scattering problems," *IEEE Antennas Wireless Propag. Lett.*, vol. 8, pp. 645–648, 2009.

[19] S. Caorsi, A. Massa, and M. Pastorino, "A computational technique based on a real-coded genetic algorithm for microwave imaging purposes," *IEEE Trans. Geosci. Remote Sensing*, vol. 38, no. 4, pp. 1697–1708, 2000.

[20] P. Rocca, M. Benedetti, M. Donelli, D. Franceschini, and A. Massa, "Evolutionary optimization as applied to inverse scattering problems," *Inverse Prob.*, vol. 25, no. 12, p. 123003, 2009.

[21] M. Donelli, G. Franceschini, A. Martini, and A. Massa, "An integrated multiscaling strategy based on a particle swarm algorithm for inverse scattering problems," *IEEE Trans. Geosci. Remote Sensing.*, vol. 44, no. 2, pp. 298–312, Feb. 2006.

[22] P. Mojabi and J. LoVetri, "Microwave biomedical imaging using the multiplicative regularized Gauss-Newton inversion," *IEEE Antennas Wireless Propag. Lett.*, vol. 8, pp. 645–648, 2009.

[23] I. T. Rekanos, T. V. Yioultsis, and T. D. Tsiboukis, "Inverse scattering using the finite-element method and a nonlinear optimization technique," *IEEE Trans. Microwave Theory Tech.*, vol. 47, no. 3, pp. 336–344, Mar. 1999.

[24] R. Kleinman and P. Berg, "A modified gradient method for two-dimensional problems in tomography," *J. Comp. Appl. Math.*, vol. 42, no. 1, pp. 17–35, 1992.

[25] P. M. van den Berg and R. E. Kleinman, "A contrast source inversion method," *Inverse Prob.*, vol. 13, no. 6, p. 1607, 1997.

[26] P. M. van den Berg, A. L. van Broekhoven, and A. Abubakar, "Extended contrast source inversion," *Inverse Prob.*, vol. 15, no. 5, p. 1325, 1999.

[27] R. Bloemenkamp, A. Abubakar, and P. Berg, "Inversion of experimental multi-frequency data using the contrast source inversion method," *Inverse Prob.*, vol. 17, p. 1611, 2001.

[28] M. Li, A. Abubakar, and P. van den Berg, "Application of the multiplicative regularized contrast source inversion method on 3D experimental Fresnel data," *Inverse Prob.*, vol. 25, p. 024006, 2009.

[29] A. Abubakar, W. Hu, P. van den Berg, and T. Habashy, "A finite-difference contrast source inversion method," *Inverse Prob.*, vol. 24, p. 065004, 2008.

[30] P. Mojabi and J. LoVetri, "Eigenfunction contrast source inversion for circular metallic enclosures," *Inverse Prob.*, vol. 26, no. 2, p. 025010, 2010.

[31] G. Otto and W. Chew, "Inverse scattering of H_z waves using local shape-function imaging: A T-matrix formulation," *Int. J. Imaging Syst. Technol.*, vol. 5, no. 1, p. 22, 1994.

[32] J. Volakis, A. Chatterjee, and L. Kempel, *Finite Element Method for Electromagnetics: Antennas, Microwave Circuits, and Scattering Applications*. New York: Wiley-IEEE Press, 1998.

[33] J. Webb, "Edge elements and what they can do for you," *IEEE Trans. Magn.*, vol. 29, no. 2, pp. 1460–1465, 1993.

[34] J. Lee, D. Sun, and Z. Cendes, "Full-wave analysis of dielectric waveguides using tangential vector finite elements," *IEEE Trans. Microwave Theory Tech.*, vol. 39, no. 8, pp. 1262–1271, 1991.

[35] H. Whitney, "Geometric integration theory," *Bull. Amer. Math. Soc.*, vol. 2, no. 9904, pp. 10143–3, 1958, .

[36] J. Nédélec, "Mixed finite elements in $\mathbb{R}^3$," *Numerische Mathematik*, vol. 35, no. 3, pp. 315–341, 1980.

[37] Z. Csendes and P. Silvester, "Numerical solution of dielectric loaded waveguides: I-finite-element analysis," *IEEE Trans. Microwave Theory Tech.*, vol. 18, no. 12, pp. 1124–1131, 1970.

[38] J. Jin, *The Finite Element Method in Electromagnetics*. New York: Wiley, 2002.

[39] P. M. van den Berg, A. Abubakar, and J. Fokkema, "Multiplicative regularization for contrast profile inversion," *Radio Sci.*, vol. 38, no. 2, p. 23, 2003.

[40] C. Gilmore, A. Abubakar, W. Hu, T. Habashy, and P. van den Berg, "Microwave biomedical data inversion using the finite-difference contrast source inversion method," *IEEE Trans. Antennas Propag.*, vol. 57, no. 5, pp. 1528–1538, May 2009.

[41] A. Abubakar, P. M. van den Berg, and J. J. Mallorqui, "Imaging of biomedical data using a multiplicative regularized contrast source inversion method," *IEEE Trans. Microwave Theory Tech.*, vol. 50, no. 7, pp. 1761–1777, Jul. 2002.

[42] A. Abubakar, P. M. van den Berg, and S. Y. Semenov, "A robust iterative method for born inversion," *IEEE Trans. Geosci. Remote Sensing*, vol. 42, no. 2, pp. 342–354, Feb. 2004.

[43] J. Geffrin, P. Sabouroux, and C. Eyraud, "Free space experimental scattering database continuation: Experimental set-up and measurement precision," *Inverse Prob.*, vol. 21, pp. S117–S117, 2005.

[44] P. Mojabi, C. Gilmore, A. Zakaria, and J. LoVetri, "Biomedical microwave inversion in conducting cylinders of arbitrary shapes," in *Proc. 13th Int. Symp. on Antenna Technology and Applied Electromagnetics and the Canadian Radio Science Meeting*, Feb. 2009, pp. 1–4.

Amer Zakaria (S'05–M'12) received the B.Sc. degree in electrical engineering (with highest honor—*summa cum laude*) from the American University of Sharjah, United Arab Emirates, in 2005, the M.Sc. degree in microwave engineering (with high distinction) from Munich University of Technology, Munich, Germany, in 2007, and the Ph.D. degree in electrical engineering from the University of Manitoba, Winnipeg, Canada, in March 2012.

From 2006 and 2007, he was working with the RF verification department in Infineon Technologies, Munich, Germany. He currently is a Postdoctoral Fellow with the Department of Electrical and Computer Engineering, University of Manitoba, Winnipeg, MB, Canada. His research interests include inverse problems, computational electromagnetics, and the development of microwave imaging systems.

Joe LoVetri (S'84–M'84–SM'09) received the B.Sc. (with distinction) and M.Sc. degrees in electrical engineering and the M.A. degree in philosophy from the University of Manitoba, Winnipeg, MB, Canada, in 1984, 1987, and 2006, respectively, and the Ph.D. degree in electrical engineering from the University of Ottawa, Ottawa, ON, Canada, in 1991.

From 1984 to 1986, he was an EMI/EMC Engineer at Sperry Defence Division, Winnipeg, and from 1986 to 1988 he held the position of TEMPEST Engineer at the Communications Security Establishment in Ottawa. From 1988 to 1991, he was a Research Officer at the Institute for Information Technology, National Research Council of Canada. His academic career began in 1991 when he joined the Department of Electrical and Computer Engineering, The University of Western Ontario, where he remained until 1999. In 1997/98, he spent a sabbatical year at the TNO Physics and Electronics Laboratory, The Netherlands, doing research in time-domain computational methods and ground penetrating RADAR. In 1999, he joined the University of Manitoba where he is currently a Professor in the Department of Electrical and Computer Engineering. From 2004 to 2009, he was the Associate Dean (Research and Graduate Programs) for the Faculty of Engineering. His main research interests lie in the areas of time-domain computational electromagnetics, modeling of electromagnetic compatibility problems, inverse problems, and biomedical imaging.

Dr. LoVetri is a Registered Professional Engineer in the province of Ontario since 1994. He received the URSI Young Scientist Award in 1993. He received the 2000 IEEE EMC Best Symposium Paper Award, and the 2007 ACES Outstanding Paper Award. In 2002 he received the University of Manitoba Rh Award for Outstanding Contributions to Scholarship and Research in the Applied Sciences. From 2005–2009 he was the National Representative for Commission E on the Canadian National Committee of URSI. In 2010 he cochaired the Ultrawideband and Short-Pulse Electromagnetics Conference which was part of AMEREM 2010 in Ottawa. He has been Chapter Chair for the IEEE EMC Ottawa Chapter as well as the Winnipeg Waves Chapter (AP/MTT).